Particle Filter for Fault Diagnosis and Robust Navigation of Underwater Robot

Bo Zhao, Roger Skjetne, Mogens Blanke, and Fredrik Dukan

Abstract—A particle filter (PF)-based robust navigation with fault diagnosis (FD) is designed for an underwater robot, where 10 failure modes of sensors and thrusters are considered. The nominal underwater robot and its anomaly are described by a switching-mode hidden Markov model. By extensively running a PF on the model, the FD and robust navigation are achieved. Closed-loop full-scale experimental results show that the proposed method is robust, can diagnose faults effectively, and can provide good state estimation even in cases where multiple faults occur. Comparing with other methods, the proposed method can diagnose all faults within a single structure, it can diagnose simultaneous faults, and it is easily implemented.

Index Terms—Fault diagnosis (FD), fault tolerance, particle filter (PF), remotely operated underwater vehicle (ROV), switch-mode hidden Markov model (HMM), underwater navigation.

I. INTRODUCTION

DUE TO the increasing requirements on safety, reliability, and availability, fault tolerant control systems design has drawn significant attention. This methodology aims to prevent that a minor fault in a component leads to loss of system functionality. Since fail-operational architectures are costly, a fault tolerant architecture is a natural choice for system design [1]. Toward realization of a fault tolerant system, the first step is to diagnose faults, where the term fault diagnosis (FD) includes fault detection, isolation, and estimation.

Model-based analytical FD is discussed in detail in [1]–[3]. Residual signals in FD are functions of the inputs and measurements of the system and a fault is detected whenever the residual exceeds a predesigned threshold. This method is practical and has many applications, such as a detailed fault tolerant design for ship propulsion in [4] and fault tolerant design for station-keeping in [5].

Classical techniques in combined state and parameter estimation include the Kalman filter and the extended Kalman filter (see [6] for linear systems, and extended to a class

B. Zhao, R. Skjetne, and F. Dukan are with the Centre for Ships and Ocean Structures, Department of Marine Technology, Norwegian University of Science and Technology, Trondheim 7491, Norway (e-mail: bo.zhao@ntnu.no; roger.skjetne@ntnu.no; fredrik.dukan@ntnu.no).

M. Blanke is with the Department of Electrical Engineering, Technical University of Denmark, Kgs. Lyngby 2800, Denmark, and also with AMOS CoE, Department of Engineering Cybernetics, Norwegian University of Science and Technology, Trondheim 7491, Norway (e-mail: mb@elektro.dtu.dk).

of nonlinear systems in [7]). FD based on combined state and parameter estimation were discussed in [8]. Observers for nonlinear systems in using estimated faults as states and sliding mode techniques were suggested in [9]. An unscented Kalman filter (UKF)-based method was developed in [10] to detect and isolate both temperature sensor and valve faults.

Particle filters (PFs) [11], [12] inherited from the Bayesian estimation and the Monte Carlo method, can also be used for this purpose. In [13], the authors developed a method that combined state estimation by a PF in a multiple model environment and likelihood ratio approach to detect and isolate faults in stochastic nonlinear systems.

Another approach using PFs for fault diagnosis was presented in [14], suggesting a hidden Markov model (HMM) with variable transition probabilities that were estimated online from data and applied to multisensor fusion for land vehicle positioning. The underwater vehicle problem is quite different. Artifacts in sensor signals, such as outliers and temporal dropouts of signals occur frequently and are essential to consider to obtain robust navigation. Another application of using a PF in fault detection is [15]. In this brief, the fault detection problem for a space rover was studied, and the so-called risk sensitive PF and variable resolution PF were reported. PFs have also been used for failure prognosis (see [16] that dealt with crack growth prediction).

This brief employs a switching-mode HMM as system description. Failure modes are included in the model, and a method is suggested using a PF to solve the FD problem on this model, hereafter called an FDPF design. The computational burden of the approach by [14] is eased significantly by formulating a model with prior and fixed probabilities of failure modes. This brief discusses how to design for a tradeoff between false alarm and detection probabilities, and it describes how this is implemented. The resulting algorithm is shown to be compact, easy to implement, and resulting in moderate computational complexity that makes the algorithm run with ease in real-time. Having introduced the PF design, this brief focus on the realization of a robust FDPF design for a remotely operated underwater vehicle (ROV). A prototype implementation is described together with results from experiments in full scale at sea where the algorithm was used in closed loop control of the ROV Minerva belonging to the Applied Underwater Robotics Laboratory (AUR-Lab) at Norwegian University of Science and Technology.

ROVs are widely used in various safety critical operations, where accurate positioning and control of the ROVs are required. It is necessary to realize high precision and fault tolerant ROV navigation. Applications of ROV integrated navigation are reported in [17] and [18]. Sensor and actuator faults are encountered frequently in practice [19];
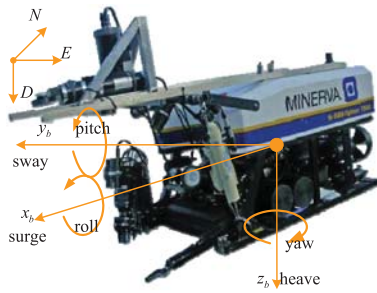
Fig. 1. ROV Minerva with kinematics notations. It has one lateral thruster, two longitudinal thrusters, and two vertical thrusters. Photo: Johanna Jarnegren.

hence, fault detection and fault handling are essential for ROV reliability. For instance, the update intervals of ROV position measurement are relatively long and uneven. This phenomenon combined with frequent outliers makes the navigation problem more complex. Detection of actuator faults and faults in navigation sensors are considered as a combined problem in this brief, and experimental data are used to assess the occurrence of different fault types. Actuator reconfiguration possibilities are rather limited on the vessel considered and are not within the scope of this brief.

This brief is organized as follows. Section II describes the model of the ROV used in the experiment and its failure modes. Section III, presents the switched HMM, the PF and the navigation system design. Results from ROV sea trials are presented in Section IV.

II. PROBLEM DESCRIPTION

A. ROV and ROV Control System

The ROV Minerva [18], as shown in Fig. 1, is a SUB-fighter 7500 ROV. It is powered from and communicates with a surface supply vessel through a 600-m umbilical cable. Minerva is equipped with five thrusters and various navigation sensors. A hydroacoustic positioning reference (HPR) system, is used to measure the position of the ROV relative to a transducer on the surface vessel. A Doppler velocity log (DVL) is installed to measure the ROV velocity. An inertial measurement unit (IMU) provides turn rate and heading measurements. Depth is provided by the HPR and also by a pressure gauge.

1) Kinematics: Adopting the notations of [20], the kinematics is described by the degrees-of-freedom (DoF) in Table I. The ROV is designed to be passive and stable in roll and pitch, the dynamics in these DoF are ignored. The kinematic model of the ROV is then given by the 4-DoF model

$$\dot{\boldsymbol{\eta}} = \boldsymbol{R}(\psi)\boldsymbol{v} \qquad (1)$$

where $\boldsymbol{\eta} = [\text{NED } \psi]^\top$ is the ROV position and heading in the North–East–Down (NED) reference frame, $\boldsymbol{v} = [u\,v\,w\,r]^\top$ is the body-fixed velocity and yaw rate vector, and $\boldsymbol{R}(\psi)$ is the rotation matrix, which transforms a vector in the ROV body frame to NED frame coordinates.

2) Kinetics: Following [20] and [18], the ROV dynamics is

$$\boldsymbol{M}\dot{\boldsymbol{v}} = -\boldsymbol{C}(\boldsymbol{v})\boldsymbol{v} - \boldsymbol{D}(\boldsymbol{v}_r)\boldsymbol{v}_r - \boldsymbol{g}(\boldsymbol{\eta}) + \boldsymbol{\tau} + \boldsymbol{w}_\nu \qquad (2)$$

$$\dot{\boldsymbol{v}}_c = -\boldsymbol{T}_c^{-1}\boldsymbol{v}_c + \boldsymbol{w}_c \qquad (3)$$

TABLE I
NOTATIONS FOR ROV MODEL

DOF	Force and moment	Linear and angular velocities	Positions and Euler angles
motion in x_b direction (surge)	X	u	N
motion in y_b direction (sway)	Y	v	E
motion in z_b direction (heave)	Z	w	D
rotation about x_b axis (roll)	K	p	ϕ
rotation about y_b axis (pitch)	M	q	θ
rotation about z_b axis (yaw)	N	r	ψ

where $\boldsymbol{M}$ is the combined rigid body and added mass matrix, $\boldsymbol{C}(\boldsymbol{v})\boldsymbol{v}$ is the Coriolis and centripetal force, $\boldsymbol{D}(\boldsymbol{v}_r)\boldsymbol{v}_r$ is the nonlinear and linear hydrodynamic damping, $\boldsymbol{g}(\boldsymbol{\eta})$ is the restoring force, $\boldsymbol{\tau} = [X\,Y\,Z\,N]^\top$ is the control force and moment, and $\boldsymbol{w}_\nu$ is process noise. All the matrices are in $\mathbb{R}^{4\times4}$, and vectors are in $\mathbb{R}^4$. In addition, $\boldsymbol{v}_r = \boldsymbol{v} - \boldsymbol{v}_c$ is the relative velocity vector with respect to the current. The current velocity $\boldsymbol{v}_c$ can be modeled as (3), where $\boldsymbol{T}_c$ is a diagonal matrix, and $\boldsymbol{w}_c$ is process noise.

B. Sensor Modeling and Anomaly Analysis

1) HPR System: The HPR system determines the position of an underwater target. The HPR measurement is a vector with North and East positions[1] and follows a multivariate Gaussian distribution:

$$p(\boldsymbol{p}_{A,k}|\boldsymbol{\eta}_k) = \mathcal{N}([\boldsymbol{I}_{2\times2}\ \ \boldsymbol{0}_{2\times2}]\boldsymbol{\eta}_k, \boldsymbol{\Sigma}_{A,k}) \qquad (4)$$

where $\mathcal{N}$ denotes the Gaussian distribution function and $\boldsymbol{\Sigma}_{A,k}$ is the covariance of the measurement noise.

When the ROV dives down to deeper water, the HPR update rate becomes nonuniform and lower than nominal. This phenomenon is named HPR dropout and is given the symbol $\Delta^{\text{HPR},1}$. In the HPR data logs, as shown in Fig. 2, the HPR update intervals were uneven and larger than 1 s in general. This is much lower than the sampling time of the control system. The HPR dropout is modeled as

$$p(\boldsymbol{p}_{A,k}|\boldsymbol{\eta}_k) = \mathcal{N}([0\ \ 0]^\top, \sigma_{A,d}^2\boldsymbol{I}) \qquad (5)$$

where $\sigma_{A,d}$ is assigned to a very large positive number representing that the current measurement is noninformative. Fig. 2 also indicates that the HPR measurement frequently suffers from outliers, which is given the symbol $\Delta^{\text{HPR},2}$.

The outliers are seen as samples from

$$p(\boldsymbol{p}_{A,k}|\boldsymbol{\eta}_k) = \mathcal{N}([\boldsymbol{I}_{2\times2}\ \ \boldsymbol{0}_{2\times2}]\boldsymbol{\eta}_k, \ \sigma_{A,o}^2\boldsymbol{I}) \qquad (6)$$

where $\sigma_{A,o}^2\boldsymbol{I}$ is the covariance of the distribution of the outliers, conceptually chosen as $\|\sigma_{A,o}^2\boldsymbol{I}\| \gg \|\boldsymbol{\Sigma}_A\|$.

2) Doppler Velocity Log: The DVL is used to measure the velocity of the ROV in 3-D space with respect to sea bottom. We used only the two horizontal components in its measurement. The DVL measurement is transformed into the ROV body frame according to

$$\boldsymbol{v}_D = \boldsymbol{R}_{\text{DVL}}^{\text{ROV}}\left(\boldsymbol{v}_D^{\text{DVL}} + r\boldsymbol{b}_{\text{DVL}}^{\text{ROV}}\right) \qquad (7)$$

---

[1]The pressure gauge depth sensor gives more reliable measurements than the HPR measurement in depth, so the depth component in the HPR measurement was not used.
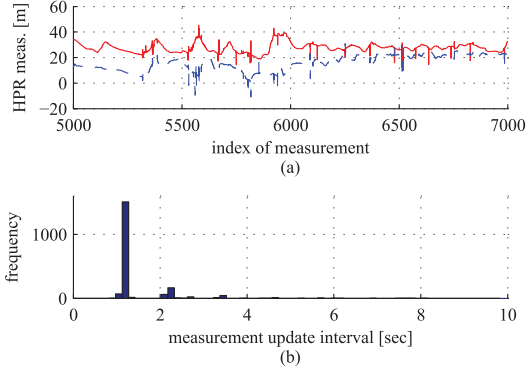
Fig. 2. (a) Segment of the HPR measurement with the measurement index along the horizontal axis. (b) Histogram of the update intervals of the HPR measurement.

where $\boldsymbol{v}_D^{\mathrm{DVL}}$ is the velocity measurement in the DVL instrument frame, $\boldsymbol{R}_{\mathrm{DVL}}^{\mathrm{ROV}}$ is the rotation matrix from the instrument frame to the body frame, $\boldsymbol{b}_{\mathrm{DVL}}^{\mathrm{ROV}}$ is the lever arm between the two frames expressed in body frame, and $\boldsymbol{v}_D$ is the resulting ROV velocity measurement in the body frame.

The DVL measurement is simply expressed as $\boldsymbol{v}_D = [u_D \; v_D]^\top$. Assuming the DVL measurement noise in each direction is independently identically normally distributed, the resulting DVL measurement $\boldsymbol{v}_{D,k}$ is

$$p(\boldsymbol{v}_{D,k}|\boldsymbol{v}_k) = \mathcal{N}\big([\boldsymbol{I}_{2\times2} \; \boldsymbol{0}_{2\times2}]\boldsymbol{v}_k, \, \sigma_D^2\boldsymbol{I}\big). \tag{8}$$

The DVL dropout problem, which is given the symbol $\Delta^{\mathrm{DVL},1}$, happens when the DVL looses sea bottom tracking. It reports a sentinel max velocity that indicates a lost velocity measurement. The DVL dropout is

$$p(\boldsymbol{v}_{D,k}|\boldsymbol{v}_k) = \mathcal{N}\big([0 \; 0]^\top, \, \sigma_{D,d}^2\boldsymbol{I}\big) \tag{9}$$

where $\sigma_{D,d}^2$ is a large positive number. The DVL measurement may suffer from a bias. For instance, an alignment error in the instrument frame can cause a bearing and offset error of the measured velocity. This failure is given the symbol $\Delta^{\mathrm{DVL},2}$.

The size of this error is unknown and time-varying, and a first-order Markov process is used to model DVL bias

$$\dot{\boldsymbol{b}}_{\mathrm{DVL}} = -\boldsymbol{T}_{\mathrm{DVL}}^{-1}\boldsymbol{b}_{\mathrm{DVL}} + \boldsymbol{w}_{\mathrm{DVL}} \tag{10}$$

where $\boldsymbol{b}_{\mathrm{DVL}} \in \mathbb{R}^2$ is the bias, $\boldsymbol{T}_{\mathrm{DVL}}$ is a diagonal time constant matrix, and $\boldsymbol{w}_{\mathrm{DVL}} \in \mathbb{R}^2$ is the driving noise. It follows that $\boldsymbol{v}_D$ is biased from the ROV velocity according to:

$$p(\boldsymbol{v}_{D,k}|\boldsymbol{v}_k, \boldsymbol{b}_{\mathrm{DVL}}) = \mathcal{N}\big([\boldsymbol{I}_{2\times2} \; \boldsymbol{0}_{2\times2}]\boldsymbol{v}_k + \boldsymbol{b}_{\mathrm{DVL}}, \, \sigma_D^2\boldsymbol{I}\big). \tag{11}$$

3) IMU and Depth Sensors: The ROV is also equipped with an IMU as heading sensor and a depth sensor, such that

$$\psi_{M,k} = [0 \; 0 \; 0 \; 1]\,\boldsymbol{\eta}_k \tag{12}$$
$$D_{P,k} = [0 \; 0 \; 1 \; 0]\,\boldsymbol{\eta}_k. \tag{13}$$

C. Thruster Control and Thruster Faults

1) Thruster Control: The Minerva ROV has five thrusters, lateral (l), vertical port (vp), vertical starboard (vs), longitudinal port (p), and longitudinal starboard (s). The thruster control, described in [18], models the achieved thrust by

$$\boldsymbol{\tau} = \boldsymbol{T}\boldsymbol{K}\boldsymbol{u} \tag{14}$$

where $\boldsymbol{T} \in \mathbb{R}^{4\times5}$ is a thrust allocation matrix that reflects thruster position and orientation, $\boldsymbol{K} \in \mathbb{R}^{5\times5}$ is a diagonal gain matrix, and $\boldsymbol{u} \in \mathbb{R}^5$ is the thrust rotational speed command from the controller. Since the thruster speed control is open-loop due to lacking rotational speed sensors, an unknown error between the commanded and actual speed of each thruster could be present. We categorize the thruster anomalies into the following failure modes.

1) The actual rotational speed is slightly lower than commanded. Such a fault is typically negligible, as it is handled by integral action.
2) The actual speed is much lower than the commanded value. We assign it mode $\Delta^{\mathrm{THR},t,1}$, where $t \in \{l, vp, vs, p, s\}$ is the thruster index.
3) The actual speed is zero, e.g., due to blocking the propeller. We name this failure mode zero thrust and assign it mode $\Delta^{\mathrm{THR},t,2}$.

We augment the state space with the vector $\boldsymbol{\alpha} = [a_l \; a_{vp} \; a_{vs} \; a_p \; a_s] \in [0, 1]^5$ to model the thrust loss, whose entries represent the ratio between the desired thrust and the actual thrust for the five thrusters. It follows for the fault-free case that all entries of $\boldsymbol{\alpha}_k$ are 1. Inserting this into the thruster model (14) yields

$$\boldsymbol{\tau} = \mathrm{diag}\{\boldsymbol{\alpha}\}\,\boldsymbol{T}\boldsymbol{K}\boldsymbol{u}. \tag{15}$$

D. Resulting ROV Model

Collecting the ROV kinematics (1), kinetics (2), current (3), the measurements (4), (8), (12), and (13), and thruster control (14), (15), we obtain the ROV model as

$$\dot{\boldsymbol{\eta}} = \boldsymbol{R}(\psi)\boldsymbol{v} \tag{16a}$$

$$\boldsymbol{M}\dot{\boldsymbol{v}} = -\boldsymbol{C}(\boldsymbol{v})\boldsymbol{v} - \boldsymbol{D}(\boldsymbol{v}_r)\boldsymbol{v}_r - \boldsymbol{g}(\boldsymbol{\eta}) + \mathrm{diag}\{\boldsymbol{\alpha}\}\boldsymbol{T}\boldsymbol{K}\boldsymbol{u} + \boldsymbol{w}_v \tag{16b}$$

$$\dot{\boldsymbol{v}}_c = -\boldsymbol{T}_c^{-1}\boldsymbol{v}_c + \boldsymbol{w}_c \tag{16c}$$

$$\dot{\boldsymbol{b}}_{\mathrm{DVL}} = -\boldsymbol{T}_{b_{\mathrm{DVL}}}^{-1}\boldsymbol{b}_{\mathrm{DVL}} + \boldsymbol{w}_{b_{\mathrm{DVL}}} \tag{16d}$$

$$p(a_{t,k}) = \begin{cases} \rho(a_{t,k}-1), & [\Delta^{\mathrm{THR},t,1}\,\Delta^{\mathrm{THR},t,2}] = [00] \\ U(0,1), & [\Delta^{\mathrm{THR},t,1}\,\Delta^{\mathrm{THR},t,2}] = [10] \\ \rho\,(a_{t,k}), & [\Delta^{\mathrm{THR},t,1}\,\Delta^{\mathrm{THR},t,2}] = [01] \end{cases} \tag{16e}$$

$$p(\boldsymbol{p}_A|\boldsymbol{\eta}) = \begin{cases} \mathcal{N}([\boldsymbol{I}\;\boldsymbol{0}]\boldsymbol{\eta}, \boldsymbol{\Sigma}_A), & [\Delta^{\mathrm{HPR},1}\,\Delta^{\mathrm{HPR},2}] = [00] \\ \mathcal{N}([0\;0]\boldsymbol{\eta}, \sigma_{A,d}^2\boldsymbol{I}), & [\Delta^{\mathrm{HPR},1}\,\Delta^{\mathrm{HPR},2}] = [10] \\ \mathcal{N}([\boldsymbol{I}\;\boldsymbol{0}]\boldsymbol{\eta}, \sigma_{A,o}^2\boldsymbol{I}), & [\Delta^{\mathrm{HPR},1}\,\Delta^{\mathrm{HPR},2}] = [01] \end{cases} \tag{16f}$$

$$p(\boldsymbol{v}_D|\boldsymbol{v}) = \begin{cases} \mathcal{N}([\boldsymbol{I}\;\boldsymbol{0}]\boldsymbol{v} + \boldsymbol{b}_{\mathrm{DVL}}, \sigma_D^2\boldsymbol{I}), & \Delta^{\mathrm{DVL},1} = 0 \\ \mathcal{N}([0\;0]\boldsymbol{\eta}, \sigma_{D,\mathrm{d}}^2\boldsymbol{I}), & \Delta^{\mathrm{DVL},1} = 1 \end{cases} \tag{16g}$$

where $\rho(\cdot)$ is the Dirac delta function.

III. PF-Based ROV Robust Navigation

A FDPF-based ROV robust navigation system is outlined in this section, introducing first some elements of the theory of FD of switching-mode hidden Markov chain models, and then focusing on the particular implementation for navigation filter design, which has some novel elements.

This article has been accepted for inclusion in a future issue of this journal. Content is final as presented, with the exception of pagination.

4   IEEE TRANSACTIONS ON CONTROL SYSTEMS TECHNOLOGY

A. Generalized Model for the System With Possible Faults

We describe a system with possible failure modes by a switching-mode HMM. This is a combined model of a first-order Markov chain representing the mode transitions, and a bank of HMMs representing the fault-free system model and the models associated with different failure modes, that is

$$\Pr(\boldsymbol{\Delta}_{k+1} = \boldsymbol{\delta}^j | \boldsymbol{\Delta}_k = \boldsymbol{\delta}^i) = p_{ij,k} \quad (17a)$$

$$\boldsymbol{X}_{k+1} | (\boldsymbol{X}_k = \boldsymbol{x}_k, \boldsymbol{u}_k, \boldsymbol{\Delta}_k = \boldsymbol{\delta}_k) \sim p\,(\boldsymbol{x}_{k+1}\,|\boldsymbol{x}_k, \boldsymbol{u}_k, \boldsymbol{\delta}_k)$$
$$= f_k\,(\boldsymbol{x}_k, \boldsymbol{u}_k, \boldsymbol{\delta}_k) \quad (17b)$$

$$\boldsymbol{Y}_k | (\boldsymbol{X}_k = \boldsymbol{x}_k, \boldsymbol{u}_k, \boldsymbol{\Delta}_k = \boldsymbol{\delta}_k) \sim p\,(\boldsymbol{y}_k\,|\boldsymbol{x}_k, \boldsymbol{u}_k, \boldsymbol{\delta}_k)$$
$$= h_k\,(\boldsymbol{x}_k, \boldsymbol{u}_k, \boldsymbol{\delta}_k). \quad (17c)$$

Equation (17a) is the mode transition Markov chain to transfer the system between system modes, where $\boldsymbol{\Delta} = [\Delta^{f^{(1)}} \quad \Delta^{f^{(2)}} \quad \cdots \quad \Delta^{f^{(N_m)}}]^\top$ is a discrete random variable defining the system mode. The components $\Delta^{f^{(p)}} \in \{0, 1\}$ ($p \in \{1, \ldots, N_m\}$) denote whether the fault $f^{(p)}$ occurs in the system, (17b) is the process equation, and $\boldsymbol{X} \in \mathbb{R}^{N_x}$ is the state vector. Its realization is $\boldsymbol{x}$.

$\boldsymbol{u} \in \mathbb{R}^{N_u}$ is the input, $p\,(\cdot)$ is a probability density function (PDF) on $\mathbb{R}^{N_x}$, and $f_k\,(\cdot) : \mathbb{R}^{N_x} \times \mathbb{R}^{N_u} \times \{0, 1\}^{N_m} \mapsto \mathbb{R}^+$ is the state transition mapping from the states, input, and system mode at time k to the PDF of the states for time $k + 1$. Equation (17c) is called the measurement equation, where $\boldsymbol{Y} \in \mathbb{R}^{N_y}$ is a random vector representing the measurement and $\boldsymbol{y}$ is its realization. $p\,(\cdot)$ is a PDF on $\mathbb{R}^{N_y}$ and $h_k\,(\cdot) : \mathbb{R}^{N_x} \times \mathbb{R}^{N_u} \times \{0, 1\}^{N_m} \mapsto \mathbb{R}^+$ is the measurement mapping, which maps the states, input, and system mode at current time to the PDF of the measurement.

Define an augmented system state vector to consist of the system state and system mode by[2] $\boldsymbol{\xi}_k = [\boldsymbol{\delta}_k^\top \quad \boldsymbol{x}_k^\top]^\top$. Then, the system can be written as

$$p(\boldsymbol{\xi}_{k+1}|\boldsymbol{\xi}_k, \boldsymbol{u}_k) = \Pr(\boldsymbol{\Delta}_{k+1} = \boldsymbol{\delta}^i | \boldsymbol{\Delta}_k = \boldsymbol{\delta}^j)$$
$$p(\boldsymbol{x}_{k+1}|\boldsymbol{\xi}_k, \boldsymbol{u}_k) = p_{ji,k} \cdot f_k(\boldsymbol{\xi}_k, \boldsymbol{u}_k) \quad (18)$$
$$p(\boldsymbol{y}_k|\boldsymbol{\xi}_k, \boldsymbol{u}_k) = h_k(\boldsymbol{\xi}_k, \boldsymbol{u}_k). \quad (19)$$

B. PF Algorithm of the Switching-Mode HMM

Solving the FD problem in (18) and (19) includes to estimate the system mode sequence $\boldsymbol{\delta}$. Assuming for instance the sequence $\boldsymbol{\delta}$ has already been estimated and that $\Delta_i^{f^{(p)}}$ is 1 for $i = k-l, \ldots, k$, then it can be concluded that the fault $f^{(p)}$ happened at time $k - l$. The advantage of this approach is that the state estimation problem and the FD problem are solved at the same time within a single structure. We employ a PF to solve this estimation problem. The proposed PF algorithm, as shown in Fig. 3, is adapted from the sampling importance resample PF (SIR-PF) in [11]. SIR-PF is employed in this brief because of its ease of implementation. However, other PF algorithms could also be employed.

[2]From now on we do not distinguish a random variable from its realization. Both of them will be denoted by lowercase letters.
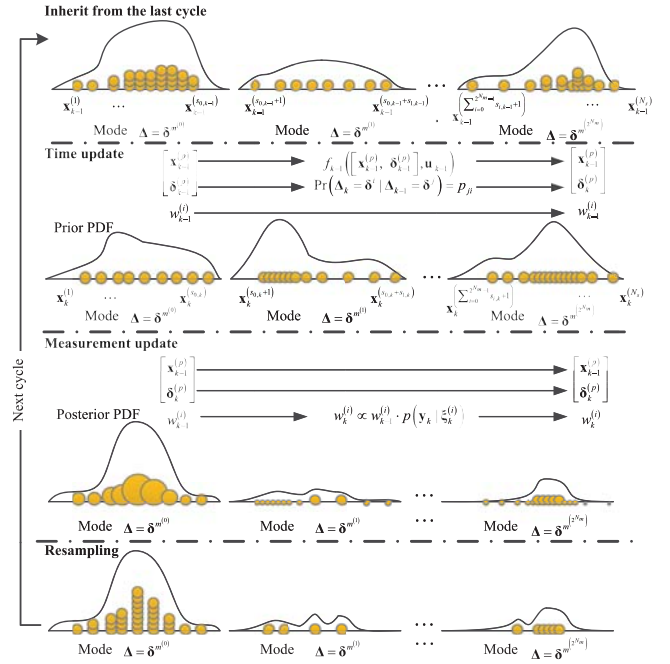

Fig. 3. One cycle of the PF, divided into three steps by chain lines. These steps corresponding to the inherit, time update, and measurement update, respectively. In the inherit step of this figure, the particles are conceptually ordered 1–N_s from left to right, for the purpose to show the replacement of the particles in the time update steps.

In the following, $\boldsymbol{x}^{(i)}$ and $\boldsymbol{\delta}^{(i)}$ denote the state vector and system mode of the ith particle, $w^{(i)}$ is the corresponding weight, and N_s is the number of particles.

1) Inheriting from the Last Cycle: The PF works in a recursive manner. At time k it inherits the posteriori estimation $p(\boldsymbol{\xi}_{k-1}|\boldsymbol{y}_{1:k-1})$. The posterior density should be understood as a combination of 2^{N_m} scaled distributions subjected to different system modes. For instance, the posteriori distribution of $\boldsymbol{x}_{k-1}$ in mode $\boldsymbol{\delta}^{m^{(q)}}$ is

$$p\big(\boldsymbol{x}_{k-1}|\boldsymbol{\Delta}_{k-1} = \boldsymbol{\delta}^{m^{(q)}}, \boldsymbol{y}_{1:k-1}\big)$$
$$\approx \frac{\sum_{i=1}^{N_s} w_{k-1}^{(i)} \cdot \rho\big(\boldsymbol{x}_{k-1} - \boldsymbol{x}_{k-1}^{(i)}\big) \cdot \rho_{\boldsymbol{\delta}^{m^{(q)}}, \boldsymbol{\delta}_{k-1}^{(i)}}}{\sum_{q=0}^{2^{N_m}-1} w_{k-1}^{(i)} \cdot \rho_{\boldsymbol{\delta}^{m^{(q)}}, \boldsymbol{\delta}_{k-1}^{(i)}}} \quad (20)$$

where $\rho\,(\cdot)$ again is the Dirac delta function, $\rho_{s,t}$ is the Kronecker delta function, and the denominator in (20) should be nonzero as long as there is at least one particle in this mode.

2) Time Update: The time update process is to obtain the a priori estimation of the states as $q(\boldsymbol{\xi}_k|\boldsymbol{\xi}_{0:k-1}, \boldsymbol{y}_{1:k})$. In the PF context, this is done by drawing samples from an importance density. The SIR-PF uses the most convenient distribution $p\big(\boldsymbol{\xi}_k|\boldsymbol{\xi}_{k-1}^{(i)}, \boldsymbol{u}_k\big)$ as the importance density. We determine the new system state by drawing samples

This article has been accepted for inclusion in a future issue of this journal. Content is final as presented, with the exception of pagination.

ZHAO *et al.*: PF FOR FD AND ROBUST NAVIGATION OF UNDERWATER ROBOT   5

from

$$p\big(\boldsymbol{\xi}_k|\boldsymbol{\xi}_{k-1}^{(i)},\boldsymbol{u}_k\big) = p\big(\boldsymbol{x}_k|\big[\boldsymbol{x}_{k-1}^{(i)},\boldsymbol{\delta}_{k-1}^{(i)}\big]^\top,\boldsymbol{u}_k\big)$$
$$\cdot \Pr\big(\boldsymbol{\delta}_k|\boldsymbol{\delta}_{k-1}^{(i)}\big). \qquad (21)$$

At the end of the time update process, the new positions $\boldsymbol{\xi}_k^{(i)}$ of the particles are obtained.

3) Measurement Update: At this step the weights of the particles are updated according to the observation $\boldsymbol{y}_k$. Given the current observation $\boldsymbol{y}_k$ and the importance density $p(\boldsymbol{\xi}_k|\boldsymbol{\xi}_{k-1}^{(i)})$, this yields

$$w_k^{(i)} \propto w_{k-1}^{(i)} \cdot p\big(\boldsymbol{y}_k|\boldsymbol{\xi}_k^{(i)},\boldsymbol{u}_k\big) \qquad (22)$$

where $p(\boldsymbol{y}_k|\boldsymbol{\xi}_k^{(i)},\boldsymbol{u}_k)$ is defined by (19).

4) Resampling: To counteract the degeneracy problem, resampling is applied following [21].

C. FD Using a PF

It is concluded that the system is in mode $\boldsymbol{\delta}^{m(q)}$ when $\boldsymbol{\Delta}_k = \boldsymbol{\delta}^{m(q)}$, termed the significant mode, has the largest marginal probability mass. This is given by

$$\max_i \Pr\big(\boldsymbol{\Delta}_k = \boldsymbol{\delta}^{m(i)}|\boldsymbol{y}_{1:k}\big) = q, \;\; i \in \{0,\dots,2^{N_m}-1\}$$

where the probability mass is obtained by marginalizing the distribution $p(\boldsymbol{\xi}_k|\boldsymbol{y}_{1:k})$, according to

$$\Pr\big(\boldsymbol{\Delta}_k = \boldsymbol{\delta}^{m(q)}|\boldsymbol{y}_{1:k}\big) \approx \sum_{i=1}^{N_s} w_k^{(j)} \rho_{\boldsymbol{\delta}^{m(q)},\boldsymbol{\delta}_k^{(i)}}. \qquad (23)$$

When the significant mode is other than fault free, a fault is detected. The particular failure is determined by the estimated system mode, meaning that the fault is isolated, and its size is obtained from the PF state estimate.

An alternative method is motivated by the CUSUM algorithm [1]. The time cumulation of the marginal masses of the modes are used as indicators, and the detection of faults is done by assessing the behavior of these indicators. This is applied to diagnose the thruster fault in Section IV-F.

D. ROV Robust Navigation System

The heave DoF can be controlled and observed separately from other DoF, since they are not coupled [20]. In addition, the corresponding sensor are reliable, so they are not included in our robust navigation design. Consequently, the failure modes regarding the two vertical thrusters are not considered in this design for simplicity.

Since the failure modes are induced by different mechanisms, it is reasonable to assume that their occurrence are independent from each other. Hence, the mode transition Markov chain can also be designed independently for each equipment and then assembled. Table II shows the mode transition probabilities for the HPR failure modes, using

$$\Pr\left(\big[\,{}_{\Delta_{k+1}^{\mathrm{HPR},1}}\,{}_{\Delta_{k+1}^{\mathrm{HPR},2}}\,\big]^\top = \boldsymbol{\delta}^{(n)}\big|\big[\,{}_{\Delta_k^{\mathrm{HPR},1}}\,{}_{\Delta_k^{\mathrm{HPR},2}}\,\big]^\top = \boldsymbol{\delta}^{(m)}\right) = p_{\boldsymbol{\delta}^{(m)}\boldsymbol{\delta}^{(n)}}. \qquad (24)$$

TABLE II
MARKOV CHAIN FOR THE TRANSITION OF MODES $\Delta^{\mathrm{HPR},1}$ AND $\Delta^{\mathrm{HPR},2}$

			$\boldsymbol{\delta}^{(m)}$		
		$\triangle^{\mathrm{HPR},1}$	0	1	0
	$p_{\boldsymbol{\delta}^{(m)}\boldsymbol{\delta}^{(n)}}$	$\triangle^{\mathrm{HPR},2}$	0	0	1
	$\triangle^{\mathrm{HPR},1}$ $\qquad$ $\triangle^{\mathrm{HPR},2}$	-	-	-	-
$\boldsymbol{\delta}^{(n)}$	0 $\qquad\qquad$ 0	-	0.75	0.75	0.75
	1 $\qquad\qquad$ 0	-	N/A	N/A	N/A
	0 $\qquad\qquad$ 1	-	0.25	0.25	0.25

TABLE III
MARKOV CHAIN FOR THE TRANSITION OF MODES
$\Delta^{\mathrm{THR},t,1}$ AND $\Delta^{\mathrm{THR},t,2}$, $t \in \{l,p,s\}$

			$\boldsymbol{\delta}^{(m)}$		
		$\triangle^{\mathrm{THR},t,1}$	0	1	0
	$p_{\boldsymbol{\delta}^{(m)}\boldsymbol{\delta}^{(n)}}$	$\triangle^{\mathrm{THR},t,2}$	0	0	1
	$\triangle^{\mathrm{THR},t,1}$ $\qquad$ $\triangle^{\mathrm{THR},t,2}$	-	-	-	-
$\boldsymbol{\delta}^{(n)}$	0 $\qquad\qquad$ 0	-	0.4	0.4	0.4
	1 $\qquad\qquad$ 0	-	0.4	0.4	0.4
	0 $\qquad\qquad$ 1	-	0.2	0.2	0.2

The transition probabilities for $\big[\,\Delta^{\mathrm{HPR},1}\;\;\Delta^{\mathrm{HPR},2}\,\big] = [1\;\;0]$ is not considered in this Markov chain since the system adopts the HPR dropout mode whenever the HPR measurement is not available in the last sampling interval.

The DVL dropout is handled as the HPR dropout, that is, the DVL measurement adopts (9), whenever its measurement is not available. The DVL bias, on the other hand, has been modeled as an additional state of the system. Hence, there is no probabilistic mode switching for the DVL.

The mode transition probabilities for the thruster modes are given in Table III, using

$$\Pr\left(\big[\,{}_{\Delta_{k+1}^{\mathrm{THR},1}}\,{}_{\Delta_{k+1}^{\mathrm{THR},2}}\,\big]^\top = \boldsymbol{\delta}^{(n)}\big|\big[\,{}_{\Delta_k^{\mathrm{THR},1}}\,{}_{\Delta_k^{\mathrm{THR},2}}\,\big]^\top = \boldsymbol{\delta}^{(m)}\right)$$
$$= p_{\boldsymbol{\delta}^{(m)}\boldsymbol{\delta}^{(n)}}. \qquad (25)$$

We then construct the system mode vector $\boldsymbol{\Delta} = \big[\,{}_{\Delta^{\mathrm{HPR},1}}\,{}_{\Delta^{\mathrm{HPR},2}}\,{}_{\Delta^{\mathrm{DVL},1}}\,\boldsymbol{\Delta}^{\mathrm{THR},1}\,\boldsymbol{\Delta}^{\mathrm{THR},2}\,\big]^\top$. The mode transition Markov chain subjects to the combination of (24) and (25) is

$$\Pr\big(\boldsymbol{\Delta}_{k+1} = \boldsymbol{\delta}^j\big|\boldsymbol{\Delta}_{k+1} = \boldsymbol{\delta}^i\big) = p_{ij}. \qquad (26)$$

The total switching-mode HMM for the ROV is obtained by combining (26) and the ROV model (16).

There are three modes for the HPR, three modes for the DVL, and we consider the three modes for the three thrusters in the horizontal plane, resulting in $3 \times 3 \times 3^3 = 243$ modes for the PF.

IV. FULL-SCALE TEST CAMPAIGN

The full-scale test was performed on October 17–18, 2012, in the Trondheimsfjord, Norway. The test was focused on the performance of the proposed FDPF-based navigation filter in a real environment, real sensor measurements, and its cooperation with the ROV control system. In addition to the FDPF-based navigation filter, a Kalman-based navigation
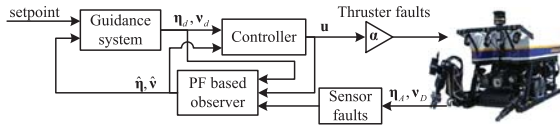
Fig. 4. Block diagram of the control system. Note that functionality has been implemented to trigger the thruster and sensors failure modes to make the failure testing more predictable and practical.

TABLE IV
PF PARAMETERS IN THE EXPERIMENT

Parameter		Value
notation	unit	
$\boldsymbol{w}_v$	[m/s]	$\sim \mathcal{N}\left(\boldsymbol{0}, 0.002\boldsymbol{I}\right)$
$\boldsymbol{T}_c$	[s]	$0.01\boldsymbol{I}$
$\boldsymbol{w}_c$	[m/s]	$\sim \mathcal{N}\left(\boldsymbol{0}, 0.01\boldsymbol{I}\right)$
$\boldsymbol{T}_{b_{\mathrm{DVL}}}$	[s]	$0.01\boldsymbol{I}$
$\boldsymbol{w}_{b_{\mathrm{DVL}}}$	[m/s]	$\sim \mathcal{N}\left(\boldsymbol{0}, 0.01\boldsymbol{I}\right)$
σ_{D}	[m²/s²]	$(0.02)^2$
$\boldsymbol{\Sigma}_{\mathrm{A}}$	[m²]	$(0.2\boldsymbol{I})^2$
$\boldsymbol{\Sigma}_{\mathrm{A,o}}$	[m²]	$(3\boldsymbol{I})^2$

filter [18] was running in parallel and open loop for comparison. Functionality has been implemented to manually set the relevant thruster and sensor failure modes according to Fig. 4 and the following.

1) HPR outliers: a random number taken from a 2-D multivariate normal distribution with zero mean and tunable variance is added to the current HPR measurement.
2) HPR dropout is triggered by blocking the measurement.
3) DVL dropout is triggered by blocking the measurement.
4) DVL bias: a tunable constant bias is added to the DVL measurement.
5) Loss of thrust: the thruster failure modes are activated by setting the gain $\boldsymbol{\alpha}_k$.

In the test trial 200 particles were used in the PF. The mode transition Markov chain probabilities are shown in Tables II and III. Other parameters were set according to Table IV. Figs. 5–9 show results from the ROV sea trial. The annotation refers to Table V. In the design, system noise is exaggerated to attenuate effects of uncertainties in hydrodynamic parameters that constitute the $\boldsymbol{C}(\boldsymbol{v})$ and $\boldsymbol{D}(\boldsymbol{v}_r)$ terms in the kinetics. This is common practice when designing observers for marine systems. Uncertainties are also attenuated by the measurement update in the PF.

A. Basic Navigation

The results of using the FDPF for state estimation of the ROV are shown in Fig. 5(a). In this test the ROV was controlled to move along a triangular path with heading along the path. It is seen that the HPR measurement suffers from outliers and low update rate. The state estimate by the FDPF is generally good, and this verifies its success as a state observer exposed to a nonuniform measurement update rate and measurement outliers. The state estimation

performance of the PF was close to the Kalman filter, but a small high-frequency oscillation was observed due to tuning.

B. Outliers

Outliers mislead the state estimation, for instance the estimation of the offline observer in Fig. 5(b) jumps after some outliers. Therefore, they have to be detected. The principle of detecting outliers embedded in the PF is just as the following hypothesis testing. Define

$$\begin{cases} \mathcal{H}_{0,k} : \text{HPR measurement at time } k \text{ is fault free} \\ \mathcal{H}_{1,k} : \text{HPR measurement at time } k \text{ is an outlier.} \end{cases}$$

It can be derived

$$\frac{\Pr\left(\mathcal{H}_{0,k}|\boldsymbol{p}_{A,k}, \hat{\boldsymbol{\eta}}_k\right)}{\Pr\left(\mathcal{H}_{1,k}|\boldsymbol{p}_{A,k}, \hat{\boldsymbol{\eta}}_k\right)} = \frac{\Pr\left(\boldsymbol{p}_{A,k}|\mathcal{H}_{0,k}, \hat{\boldsymbol{\eta}}_k\right)\Pr\left(\mathcal{H}_{0,k}\right)}{\Pr\left(\boldsymbol{p}_{A,k}|\mathcal{H}_{1,k}, \hat{\boldsymbol{\eta}}_k\right)\Pr\left(\mathcal{H}_{1,k}\right)} \quad (27)$$

where $\hat{\boldsymbol{\eta}}_k$ is the prior estimation, $\Pr\left(\mathcal{H}_{0,k}\right)$ and $\Pr\left(\mathcal{H}_{1,k}\right)$ are the transition probabilities defined in the Markov chain, and $\Pr\left(\boldsymbol{p}_{A,k}|\mathcal{H}_{0,k}, \hat{\boldsymbol{\eta}}_k\right)$ and $\Pr\left(\boldsymbol{p}_{A,k}|\mathcal{H}_{1,k}, \hat{\boldsymbol{\eta}}_k\right)$ are determined by the measurement relation (16f). In the PF the same process is implicitly done by the importance sampling (21) and the measurement update (22). This hypothesis testing is influenced by the variance of the prior estimation. Table VI shows the detectability of an outlier based on the size of the outlier and the dropout time before the outlier measurement is made. Naturally, it is more difficult to detect an outlier the longer the dropout time is, and outliers with large amplitude are more easily detected.

To test outlier detection, outliers of known amplitudes were injected during an position-keeping test. The statistics of the outlier detection is presented in Fig. 5, which coincides compares with Table VI.

C. HPR Dropout

Fig. 6(a) shows the performance of the FDPF when the HPR drops out for about 30 s while the ROV was moving straight in an Eastern direction. As discussed earlier, the HPR dropout does not have to be diagnosed since it is handled within the nonuniform sampling interval mechanism, even for such a long interval, all the while the FDPF outputs a steady stream of position estimates. In state-of-the-art observers this is typically achieved by entering a dead-reckoning mode [22], such that the position is estimated open-loop based on the thrust force and, possibly, velocity measurement. However, such an observer may fail to estimate the ROV position correctly when then HPR drops out for too long time, as seen in the large deviation between the ROV position and the offline filter estimation in Fig. 6(a). When the position measurement drops out here, the variance of the estimation cannot be reduced by new position information and the uncertainty of the estimation grows due to system noise. This is observed by the increasing distance between the upper and lower 1σ bounds. The estimated position during the dropout is shown to be close to the original fault-free measurement, and this confirms the good dead-reckoning capability of the FDPF.
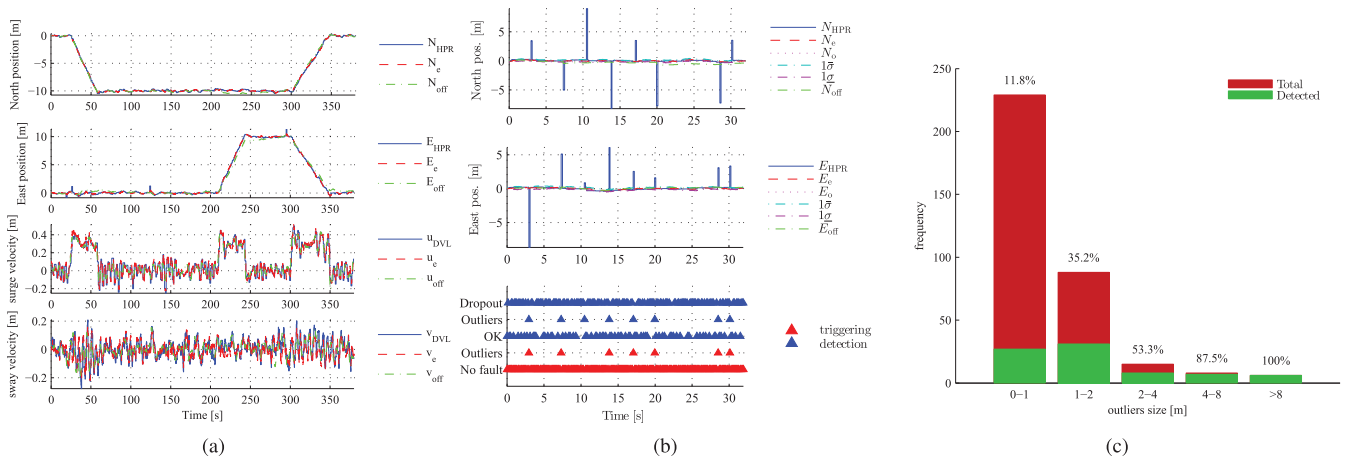
Fig. 5. (a) Measurements and state estimation when the ROV was moving along a triangular path. (b) Measurements and state estimation using HPR even during dropout. (c) State estimation after detection and removal of outliers.
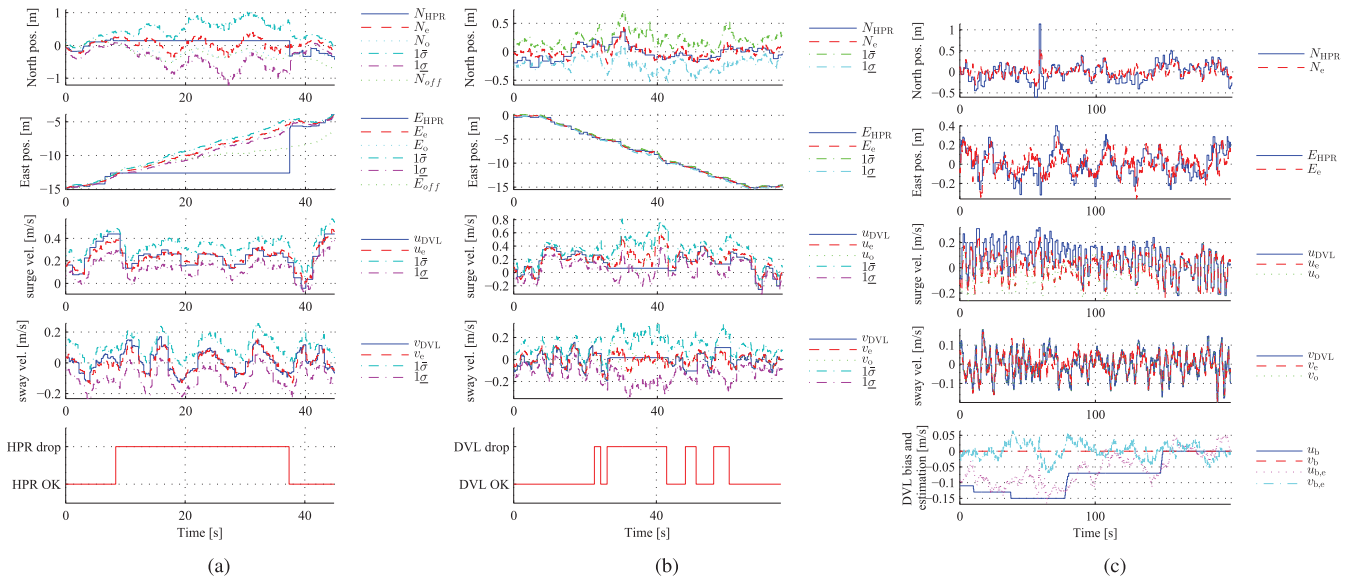

Fig. 6. (a) Measurements and state estimation subject to HPR dropouts. (b) Measurements and state estimation subject to DVL dropout. (c) Measurements and state estimation subject to DVL bias.

D. DVL Dropout

When the DVL drops out, the state estimation is based on the thrust force command and the HPR measurement. The performance of the FDPF is for this case shown in Fig. 6(b), showing that the estimated velocity is satisfactorily close to the original fault-free measured velocity during the DVL dropout. Similar to the HPR dropout case, the variance of the velocity estimation increases during the DVL dropout. However, this increase only lasts for about 3 s until it settles at a stationary value. This can be explained by the Bayesian properties of the PF. The particles with estimated velocity that are significantly different from the actual velocity will not be supported by the observations since these will also yield a large difference between the estimated position and the measured position. This is an information back propagation feature of PFs.

E. DVL Bias

In the sea trial, a DVL bias was injected in the ROV surge direction while the ROV was in position-keeping operation. The bias was first increased slowly in steps before decreased back to 0. The corresponding experimental responses are shown in Fig. 6(c). The bias estimate is close to the value of the manually triggered fault, especially if taking the variances of the DVL measurement noise and the system noise into account. This indicates that the DVL bias is well diagnosed by the algorithm.

F. Insufficient Thrust and Zero Thrust

The reduced thrust failure mode was tested by decreasing the thrust from the two surge-directed thrusters, as shown in the third graph in Fig. 9(a), in such a way as to avoid spin of the ROV.
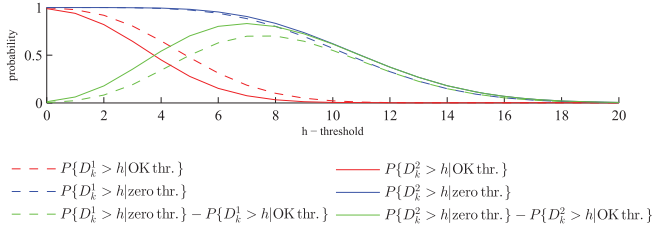
Fig. 7. Probabilities of detection P_D and false alarm P_F versus value of threshold. The difference $P_D - P_F$ is an indicator for the tradeoff between P_D and P_F.
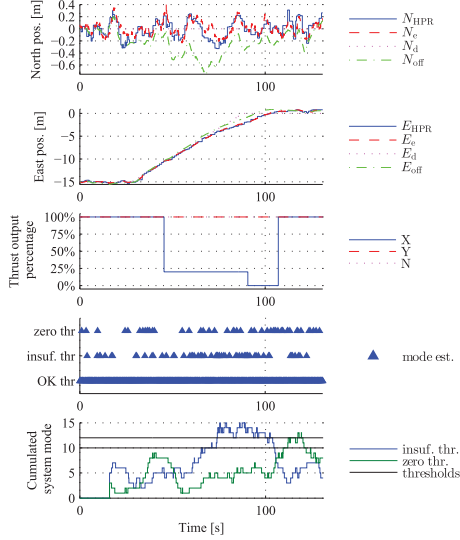

Fig. 8. Measurements and state estimate when injecting thruster faults.

TABLE V
NOTATIONS IN THE EXPERIMENTAL RESULTS FIGURES

Notation	Meaning
N, E	North and East position.
u, v	Surge and sway velocity.
subscript $\square_e$	FDPF estimate.
subscript $\square_d$	Desired position/velocity from the guidance system.
subscript $\square_o$	Measurement without triggered failure modes.
subscript $\square_{off}$	Estimation from the sector heading KF in open-loop .
$1\bar{\sigma}$	1σ upper bound of the FDPF estimate.
$1\underline{\sigma}$	1σ lower bound of the FDPF estimate.

TABLE VI
HPR OUTLIERS DETECTION

		dropout time before the outlier [s]						
		0.9	1.8	2.7	3.6	4.5	7.2	9.0
	0.4	X[3]	X	X	X	X	X	X
	0.6	◯	X	X	X	X	X	X
	1.0	◯	◯	X	X	X	X	X
outliers	1.6	◯	◯	◯	X	X	X	X
size [m]	2.4	◯	◯	◯	◯	X	X	X
	2.8	◯	◯	◯	◯	◯	X	X
	3.6	◯	◯	◯	◯	◯	◯	X
	4.0	◯	◯	◯	◯	◯	◯	◯

TABLE VII
ANALYSIS OF THRUSTER FAULT DETECTION RESULT

Thruster mode	Percentage of estimated mode		
	$\triangle^{\mathrm{THR},0}$	$\triangle^{\mathrm{THR},1}$	$\triangle^{\mathrm{THR},2}$
$\triangle^{\mathrm{THR},0}$	90.1%	5.5%	4.4%
$\triangle^{\mathrm{THR},1}$	not enough samples		
$\triangle^{\mathrm{THR},2}$	77.2%	11.2%	11.6%

The Kalman filter estimates rapidly diverged from the true state when the fault was triggered. In contrast, the FDPF provides good state estimates during presence of these failures.

When the thrust failure is present, the FDPF shows more frequent confirmation of zero thrust and insufficient thrust modes than in fault-free conditions. Table VII shows the thruster mode and estimated thruster mode during the period in Fig. 9(a), where the thruster modes are referring to the two thrusters in the surge direction.

Thus, we obtain the probabilities $\mathrm{Pr}\{\hat{\delta}_k = \triangle^{\mathrm{THR},i}|\delta_k = \triangle^{\mathrm{THR},j}\}$, $(i, j \in \{0, 1, 2\})$. Defining two statistics $D_k^i = \sum_{j=k-n}^{k} \rho(\hat{\delta}_j, \triangle^{\mathrm{THR},i})$ $(i = 1, 2)$ as the time cumulations of the estimated system modes, where n is a moving window length, we can calculate the probabilities of detection $P\{D_k^i > h|\{\delta_{k-n}, \cdots, \delta_k\}\}$, where h is a threshold to be decided by examining the false-alarm-rate and time-to-detection. As an example, Fig. 7 shows the probability of detection and false alarm against the threshold when the window size is 100 (which is 15 s). This suggests to use the thresholds 12 for $\triangle^{\mathrm{THR},1}$ and 10 for $\triangle^{\mathrm{THR},2}$ to restrain the false alarms. To this end, the fourth graph in Fig. 9(a) shows the D_k^1, D_k^2 with moving window size 100, and the threshold. The statistic D_k^1 exceeds the corresponding threshold in 16 s after the fault happens. Fig. 8 shows the result when applying this method and thresholds to another set of experiments, where a thruster fault was injected. The result validates the proposed

diagnosis method where the two statistics helps to make the fault detection robust to model uncertainty.

G. Multiple Failure Modes

Two combinations of simultaneous failures were tested. Fig. 9(b) shows the state estimation for a DVL drop-out during a HPR dropout. At the end of the 30 s HPR dropout, the position estimate has deviated about 1m from the measurement, while the velocity estimate is intact.

The other multiple failure mode test was assessing the system response to HPR outliers during a DVL dropout period, and the results are shown in Fig. 9(c). When HPR outliers occur during a DVL dropout, the variance of the position estimate becomes large, and this makes detection of outliers increasingly difficult.

The position and velocity estimation is again good. In this case one should also notice that the variance of the velocity estimation did not increase as much as in the previous multiple failure case (but more than the fault-free case) since the information from the HPR is back propagated to the velocity estimation through the system model.

---

[3] "X" means a outlier is determined to be fault-free, and "◯" means a outlier is determined to be outlier.

This article has been accepted for inclusion in a future issue of this journal. Content is final as presented, with the exception of pagination.

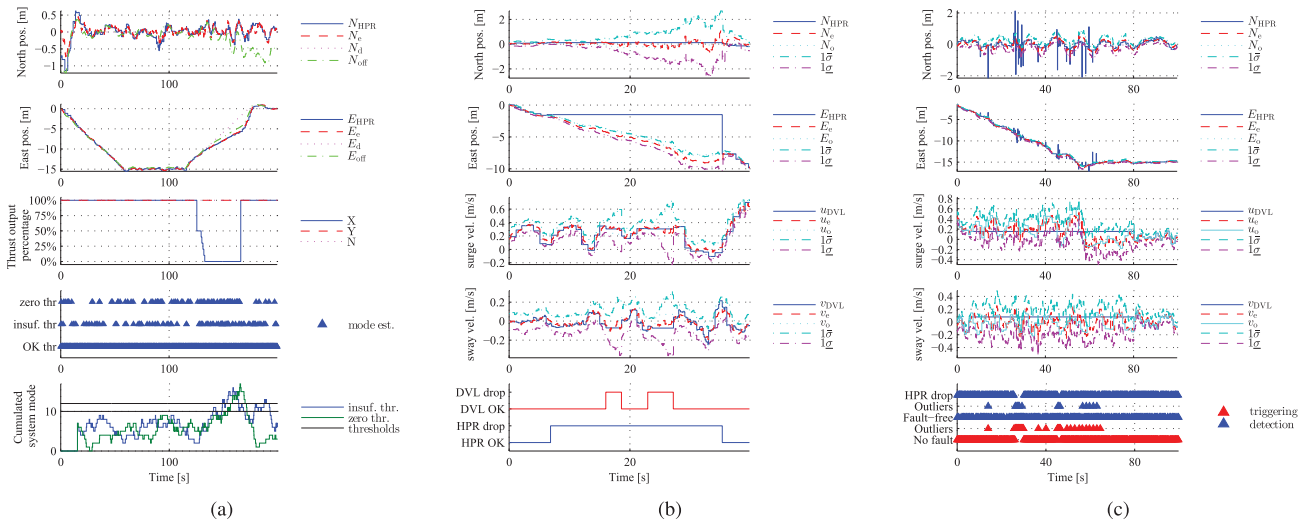ZHAO *et al.*: PF FOR FD AND ROBUST NAVIGATION OF UNDERWATER ROBOT
9

Fig. 9. (a) Measurements and state estimate when thruster faults are injected. (b) Measurements and state estimate subject to HPR dropout and DVL dropout. (c) Measurements and state estimate subjected to HPR outliers and DVL dropout.

V. CONCLUSION

In this brief, we have proposed a PF-based algorithm for FDPF built on a switching-mode HMM. The algorithm was applied to robustify the navigation of an ROV, where the navigation sensors and thrusters are vulnerable and fault diagnosis is essential. The design was tested in a full-scale ROV sea trial, for which the design process and the test responses have been presented and discussed in detail. The experimental results confirm that the performance of the fault diagnosis was generally good and that the proposed algorithm provided robust and efficient state estimation for the ROV under different combinations of failure modes, signal artifacts, and disturbances.

REFERENCES

[1] M. Blanke, M. Kinnaert, J. Lunze, and M. Staroswiecki, *Diagnosis and Fault-Tolerant Control*. New York, NY, USA: Springer-Verlag, 2006.

[2] Y. Zhang and J. Jiang, "Bibliographical review on reconfigurable fault-tolerant control systems," *Annu. Rev. Control*, vol. 32, no. 2, pp. 229–252, 2008.

[3] I. Hwang, S. Kim, Y. Kim, and C. E. Seah, "A survey of fault detection, isolation, and reconfiguration methods," *IEEE Trans. Autom. Control*, vol. 18, no. 3, pp. 636–653, May 2010.

[4] M. Blanke, R. Izadi-Zamanabadi, and T. F. Lootsma, "Fault monitoring and re-configurable control for a ship propulsion plant," *Int. J. Adapt. Control Signal Process.*, vol. 12, no. 8, pp. 671–688, 1998.

[5] M. Blanke, "Diagnosis and fault-tolerant control for ship station keeping," in *Proc. IEEE Int. Symp., Mediterrean Conf. Control Autom. Intell. Control*, Jun. 2005, pp. 1379–1384.

[6] L. Ljung, "Asymptotic behavior of the extended Kalman filter as a parameter estimator for linear systems," *IEEE Trans. Autom. Control*, vol. 24, no. 1, pp. 36–50, Feb. 1979.

[7] W.-W. Zhou and M. Blanke, "Identification of a class of nonlinear state-space models using RPE techniques," *IEEE Trans. Autom. Control*, vol. 34, no. 3, pp. 312–316, Mar. 1989.

[8] N. E. Wu, S. Thavamani, Y. Zhang, and M. Blanke, "Sensor fault masking of a ship propulsion system," *Control Eng. Practice*, vol. 14, no. 11, pp. 1337–1345, 2006.

[9] C. Edwards, S. Spurgeon, and R. Patton, "Sliding mode observers for fault detection and isolation," *Automatica*, vol. 36, no. 4, pp. 541–553, 2000.

[10] L. Shang and G. Liu, "Sensor and actuator fault detection and isolation for a high performance aircraft engine bleed air temperature control system," *IEEE Trans. Control Syst. Technol.*, vol. 19, no. 5, pp. 1260–1268, Sep. 2011.

[11] M. Arulampalam, S. Maskell, N. Gordon, and T. Clapp, "A tutorial on particle filters for online nonlinear/non-Gaussian Bayesian tracking," *IEEE Trans. Signal Process.*, vol. 50, no. 2, pp. 174–188, Feb. 2002.

[12] A. Doucet and A. Johansen, *The Oxford Handbook of Nonlinear Filtering*. Cambridge, U.K.: Cambridge Univ. Press, 2009.

[13] P. Li and V. Kadirkamanathan, "Particle filtering based likelihood ratio approach to fault diagnosis in nonlinear stochastic systems," *IEEE Trans. Syst., Man, Cybern. C, Appl. Rev.*, vol. 31, no. 3, pp. 337–343, Aug. 2001.

[14] F. Caron, M. Davy, E. Duflos, and P. Vanheeghe, "Particle filtering for multisensor data fusion with switching observation models: Application to land vehicle positioning," *IEEE Trans. Signal Process.*, vol. 55, no. 6, pp. 2703–2719, Jun. 2007.

[15] V. Verma, G. Gordon, R. Simmons, and S. Thrun, "Real-time fault diagnosis [robot fault diagnosis]," *IEEE Robot. Autom. Mag.*, vol. 11, no. 2, pp. 56–66, Jun. 2004.

[16] M. E. Orchard and G. J. Vachtsevanos, "A particle-filtering approach for on-line fault diagnosis and failure prognosis," *Trans. Inst. Meas. Control*, vol. 31, nos. 3–4, pp. 221–246, 2009.

[17] J. C. Kinsey and L. L. Whitcomb, "Preliminary field experience with the DVLNAV integrated navigation system for oceanographic submersibles," *Control Eng. Practice*, vol. 12, no. 12, pp. 1541–1549, 2004.

[18] F. Dukan, M. Ludvigsen, and A. Sørensen, "Dynamic positioning system for a small size ROV with experimental results," in *Proc. OCEANS IEEE*, Jun. 2011, pp. 1–10.

[19] G. Antonelli, "A survey of fault detection/tolerance strategies for AUVS and ROVS," in *Fault Diagnosis and Fault Tolerance for Mechatronic Systems: Recent Advances*, vol. 1, F. Caccavale and L. Villani, Eds. Berlin, Germany: Springer-Verlag, 2003, pp. 109–127.

[20] T. I. Fossen, *Handbook of Marine Craft Hydrodynamics and Motion Control*. New York, NY, USA: Wiley, 2011.

[21] J. Liu, "Metropolized independent sampling with comparisons to rejection sampling and importance sampling," *Statist. Comput.*, vol. 6, no. 2, pp. 113–119, 1996.

[22] A. Sørensen, *Marine Control Systems: Propulsion and Motion Control Systems of Ships and Ocean Structures*, 2nd ed. Trondheim, Norway: Norwegian Univ. Sci. Technol., 2012.